AIAA JOURNAL
Vol. 38, No. 12, December 2000

Numerical and Experimental Investigation of Double-Cone Shock Interactions

M. J. Wright,* K. Sinha,† J. Olejniczak,* and G. V. Candler‡
University of Minnesota, Minneapolis, Minnesota 55455
and
T. D. Magruder§ and A. J. Smits¶
Princeton University, Princeton, New Jersey 08544

A series of experiments was conducted in the Princeton University Mach 8 Wind Tunnel to study shock interactions on axisymmetric double-cone geometries. Schlieren images and surface-pressure data were taken. Two models were tested, which were expected to produce steady Type VI and Type V shock interactions. The experiments are compared to computational fluid dynamics calculations, and the features of these complicated flowfields are discussed. The comparison is excellent for the laminar Type VI shock interaction. The computations accurately reproduce the size of the separation zone and the surface pressure. However, for the Type V interaction the laminar computation overpredicts the size of the separation region. In addition, the experimental results for the Type V interaction show that the size of the separation region decreases with increasing Reynolds number, whereas the laminar computations predict the opposite trend. Turbulent computations show much better agreement with experimental data and reproduce the experimentally observed relationship between the size of the separation region and the Reynolds number, indicating that the reattachment shocks cause transition to turbulence in these flows.

Introduction

INTERACTIONS between the bow shock of a hypersonic vehicle with the shock waves generated by a wing or control surface are a vital design consideration because of the potentially high localized heat-transfer rates in the interaction region. For this reason a large amount of work has been done in an attempt to classify and predict shock interaction phenomena. The pioneering work in this field was by Edney,[1] who classified six types of shock interactions based on an experimental study of oblique shock waves impinging on a variety of blunt bodies. These classifications have since become the basis for categorizing all shock interactions.

More recently Olejniczak et al.[2] used double-wedge geometries to test different nonequilibrium chemistry models. Under certain conditions these flows produced steady large amplitude pressure variations on the body surface. Although these pressure variations were originally thought to be caused by real-gas effects, recent work by Olejniczak et al.[3,4] studying inviscid perfect gas flows over double wedges has shown that the mechanism which causes these variations can be found in the underlying gas dynamics. Olejniczak et al. identified five types of inviscid shock interactions on double-wedge geometries, including one which does not fit into the Edney classification scheme. For the cases in which steady pressure variations are observed, a Type IV or Type V shock interaction occurs, and an underexpanded supersonic jet is emitted from the triple point region. This jet is trapped against the wedge surface and undergoes a series of isentropic expansions and recompressions as the flow adjusts to match the imposed boundary conditions, leading to steady variations in the pressure and other flow quantities. These results are similar to the work of Lamont and Hunt,[5] who studied underexpanded jets impinging on inclined plates. The variations in the flow quantities can be quite large and thus can significantly impact the heat transfer and aerodynamic coefficients of the wedges.

Laminar viscous double wedges were also examined numerically in Ref. 3. These flows were shown to be considerably more complicated than the inviscid cases, primarily because of the separation zone that forms at the corner of the wedges and the resulting separation shock that interacts with the oblique shock from the nose of the first wedge. In many cases viscous effects can alter the basic nature of the interaction, making it difficult to classify these flows using Edney's scheme. However, flow patterns similar to Edney's Type V and Type VI shock interactions were observed for certain cases. These flows were steady only for a limited range of Reynolds numbers and second wedge angles. Many of the unsteady flows exhibited an oscillatory behavior similar to the spike-tipped blunt-body flows investigated by Maull.[6] Flow patterns similar to the Type IV shock interaction, with the accompanying pressure variations, were not observed for these laminar flows.

Little experimental data exist in the area of shock interactions on double-wedge or double-cone geometries. Bertin and Hinkle[7] performed an experimental investigation of the Type V and Type VI interactions on double wedges in which they prevented separation by bleeding off the boundary layer at the corner of the wedges, but it is unclear how the bleeding procedure and three-dimensional end effects impacted their results. In addition, Holden and Moselle[8] and Holden[9] and others have examined hypersonic flow over two-dimensional compression corners. These flows exhibit similar features to the double-wedge flows of interest, including the separation region at the corner and the associated separation shock, but lack the strong shock-shock interaction that is the dominant feature of the double-wedge flowfield.

In this paper we combine a series of experiments with a numerical study of viscous double-cone shock interactions. We chose axisymmetric double-cone geometries, rather than double wedges, to eliminate the possibility of three-dimensional end effects. A series of numerical calculations were undertaken to examine the large parameter space of these flows in order to identify a small number of experimental test cases. To simplify this parametric study, we examined only cases in which the lengths of the two cones are equal. From this numerical study we selected two model geometries, which were expected to produce Type VI and Type V shock interactions. These

Presented as Paper 97-0063 at the 35th Aerospace Sciences Meeting, Reno, NV, 11–14 January 1997; also as Paper 99-0146 at the 37th Aerospace Sciences Meeting, 6–9 January 1999; received 3 December 1999; revision received 21 April 2000; accepted for publication 17 May 2000.

*Postdoctoral Research Associate, Department of Aerospace Engineering and Mechanics. Member AIAA.
†Graduate Research Assistant, Department of Aerospace Engineering and Mechanics. Student Member AIAA.
‡Professor, Department of Aerospace Engineering and Mechanics. Senior Member AIAA.
§Graduate Research Assistant, Department of Mechanical and Aerospace Engineering. Student Member AIAA.
¶Professor, Department of Mechanical and Aerospace Engineering. Associate Fellow AIAA.

models were instrumented with pressure taps and run in the Princeton University Mach 8 Blowdown Wind Tunnel at two Reynolds numbers. The results are compared to computational fluid dynamics (CFD) calculations. Good agreement is obtained for the Type VI interaction using CFD. However, experimental runs of the Type V interaction show a smaller separation region than that predicted by laminar CFD. In addition, the experimental results for the Type V interaction show that the size of the separation region decreases with increasing Reynolds number, the opposite of the trend seen with laminar CFD. These cases are examined using a two-equation k–ϵ turbulence model, and the results are in much better agreement with the experiments. These results clearly demonstrate the large effect of turbulence and transition on these flows. The turbulent calculations reproduce the qualitative trends seen in the experiment and predict a size for the separation region that is much closer to the experimental value.

Experimental Setup

Facility

The experiments were conducted in the Princeton University Gas Dynamics Laboratory Mach 8 blowdown facility, which is described in detail by Baumgartner et al.[10] This wind tunnel has a 0.23-m (9-in.)-diam test section with four-way optical access. Run times of up to 2 min are possible. This facility is ideal for our purposes because it allows us to perform experiments in the high-Mach-number regime without the complications of real-gas effects. This permits us to directly examine the fluid mechanics of these flows. Two nominal run conditions were selected for the experiments: a low-Reynolds-number Re condition, with a stagnation pressure $p_0 = 3.45$ MPa (500 psi), and a high Re condition, with a stagnation pressure 6.90 MPa (1000 psi). The nominal stagnation temperature was $T_0 = 750$ K for both conditions. Freestream conditions were obtained by assuming an isentropic expansion to Mach 8 flow from these known reservoir (stagnation) values. Actual run conditions and uncertainty estimates for each case are noted in the following results; they were typically within 10% of the nominal values and varied less than 5% over the course of each run.

Models and Instrumentation

The two models each have a first-cone half-angle of 25 deg. The second-cone half-angle is 35 deg for the first model and 50 deg for the second. Both single piece brass models were originally machined with a 0.051-m (2-in.) base diameter. However, although the 25–35-deg model exhibited good tunnel starting characteristics, preliminary runs using the 25–50-deg model resulted in tunnel unstart.[11] Therefore, a new second model was constructed with a smaller 0.038-m (1.5-in.) base diameter, which allowed proper tunnel operation. The 25–35-deg double cone has equal face lengths of $L = 0.026$ m (1 in.) and a 0.038 m (1.5 in.) cylindrical afterbody following the 35-deg face. The 25–50-deg double cone has face lengths of $L = 0.016$ m (0.63 in.) and an afterbody length of 0.019 m (0.75 in.). The models were mounted to the sting using bolts screwed into the base. Before each run the test section was preheated with high-temperature air until the model reached a temperature of 540 K, which was the highest temperature possible using our preheating technique.

Each model was fitted with a pair of Omega-type K ungrounded thermocouples, with a manufacturer reported accuracy of 0.75% of reading. These thermocouples were used only to estimate the change in surface temperature during the course of the run. Pressure measurements were made with an MKS Baratron 1000 torr pressure transducer, which has a manufacturer reported accuracy of 0.15% of reading. The inside diameter of the pressure taps was 0.51 mm (0.020 in.) on the 25–35-deg model and 1.19 mm (0.047 in.) on the 25–50-deg model. Larger taps were used on the second model as a result of the long response times of the 0.51-mm taps. An estimate was made for the error in the pressure measurement caused by the inside diameter of the pressure tap. Based on the analysis of Livesey et al.,[12] it was found that the worst-case error should be about 1.5% of reading. Seven pressure taps were placed on the 25–35-deg model and nine on the 25–50-deg model. The locations of the thermocouples and pressure taps were chosen based on preliminary CFD analysis of the models at nominal run conditions. In each case four taps were distributed circumferentially around the model to verify that the flow was indeed axisymmetric.

Average pressure measurements were recorded sequentially for each tap at a rate of 1 point per second. Each tap was measured for approximately 10–20 s. Stagnation pressure and temperature were also recorded during each measurement. Because of the long response times of the 0.51-mm taps, the pressure reading behaved like the response of a first-order system to a step input. Therefore, final pressure measurements for these taps were obtained using the following equation:

$$p(t) = (p_{\text{init}} - p_{\text{final}})e^{-t/\tau} + p_{\text{final}}$$

where the constants p_{init}, p_{final}, and τ are found through a curve fit to the data. Pressure data for the larger (1.19 mm) pressure taps were obtained by averaging over the final 5 s of raw data. Because the stagnation pressure varied by as much as 5% over the course of each run, each pressure reading was normalized by the average stagnation pressure recorded during that measurement. The total estimated error in the experimentally measured normalized pressure was $\pm 3\%$ of reading caused primarily by uncertainty in the freestream conditions. The circumferentially distributed pressure taps verified that the flow during each run was indeed axisymmetric to within experimental uncertainty ($|\alpha| < 1$ deg).

The flow was also examined by means of a video schlieren system, similar to the Toepler schlieren described by Merzkirch.[13] The light source was a white strobe followed by a narrow slit. Instead of lenses, large spherical mirrors ($f = 72$ in.) were used. The strobe pulse length was approximately 2 μs, and the strobe speed was adjusted to match the 30 frames per second frame rate of the charge-coupled device (CCD) camera. The CCD video output was recorded by a commercial grade VCR and subsequently digitized using an Imaging Technology Series 151 Image Processor. The digitized images were enhanced using image-processing software to reduce noise and highlight the flow structure. Further details of the experimental procedure can be found in Ref. 14.

Numerical Method

We solve the Favre-averaged axisymmetric Navier–Stokes equations[15] for the mean flow quantities and model the effect of turbulence using the low Reynolds k–ϵ turbulence model presented by Jones and Launder.[16] This approach has been widely used for simulating high-speed compressible flows. The assumptions involved in this approach and the resulting limitations are discussed next. Laminar solutions are obtained by setting the initial freestream turbulent kinetic energy k_∞ and turbulent dissipation ϵ_∞ to zero. Freestream conditions were obtained by assuming an isentropic expansion to Mach 8 from measured stagnation values. A no-slip velocity condition was applied at the body surface, and an isothermal wall was assumed for all cases, with the wall temperature determined by an estimate of model heating obtained from the thermocouples. Computational schlieren images are generated by line-of-sight integration through the axisymmetric flowfield, following the methods described by Yates.[17]

During the solution procedure, a laminar computation is first obtained for each flow case. This solution is then combined with a uniform distribution of turbulent kinetic energy ($k = k_\infty$) and turbulent dissipation ($\epsilon = \epsilon_\infty$) throughout the flowfield to start the turbulent computation, where k_∞ is related to the freestream velocity U_∞ by assuming a turbulent intensity of 0.1% ($k_\infty = 0.001U_\infty^2$). Next, we assume that in the freestream the turbulent eddy viscosity is equal to the molecular viscosity μ_∞ and thus estimate the freestream turbulent dissipation as $\epsilon_\infty = c_\mu \rho_\infty k_\infty^2 / \mu_\infty$, where ρ_∞ is the freestream density, c_μ is a constant (0.09) in the turbulence model, and k and ϵ are set to zero at the cone surface.

The governing equations are solved using a modified form of Steger–Warming flux vector splitting,[18] which significantly reduces the dissipation of the original scheme. The MUSCL approach has been used to achieve second-order spatial accuracy in the body-tangential direction, while the body-normal direction is first-order accurate. The k–ϵ equations are solved fully coupled with the mean flow equations. The formulation is presented in Ref. 19 and has been

Table 1 Measured average stagnation and operating conditions for the 25–35-deg double-cone runs

	Low Reynolds number			High Reynolds number		
Variable	Run 1	Run 2	CFD	Run 1	Run 2	CFD
T_0, K	786 ± 3	789 ± 4	790	784 ± 11	796 ± 3	790
p_0, MPa	3.51 ± 0.01	3.56 ± 0.02	3.55	5.91 ± 0.06	6.33 ± 0.10	6.20
M_∞	7.98 ± 0.04	7.98 ± 0.04	8.00	8.07 ± 0.04	8.09 ± 0.04	8.10

validated for turbulent boundary layers on flat plates. The implicit Data-Parallel Line Relaxation method of Wright et al.[20] was used to obtain steady-state solutions. Because of the complex nature of these shock interaction flows, a large number of grid points are required to ensure a grid-converged solution. In addition, the structure of the grid, particularly around the interaction points, can influence the angles of the transmitted shocks and shear layers. In this paper care has been taken to design grids with enough points in the proper locations to ensure accurate results. Grid-convergence issues will be discussed in the next section; however, in Ref. 4 grid sizes of 1024×1024 points were required to capture the important features of some inviscid double-wedge flows. Because of the large number of grid points required, the algorithm was implemented in parallel on a Cray T3E using message passing.

The k–ϵ turbulence models were originally developed for incompressible flows. Zhang et al.[21] showed that these models along with Favre-averaged mean flow equations can be extended to high-Mach-number flows if the near-wall modifications are asymptotically consistent. Good agreement with experimental data was observed by Zhang for boundary-layer flows up to Mach 10 for adiabatic and cold walls. The k–ϵ model used in this paper also satisfies the asymptotic consistency condition.[15] Therefore the turbulence model is expected to work well for the boundary layers on the cones. On the other hand, turbulent free shear layers at high convective Mach numbers require additional compressibility corrections.[15] In the computation of these double-cone flows, all of the free shear layers are found to be laminar, both computationally and according to the transition criterion given by Birch and Keyes.[22] Therefore, the turbulence model without the compressibility corrections is expected to work well for these flows. However, there are certain limitations of the k–ϵ turbulence model. These models were developed for equilibrium turbulent flows, and they have not been validated for predicting transition. Also, the accuracy of the model predictions deteriorates in the presence of pressure gradients. Because the flows considered here appear to be transitional and there are strong pressure gradients across the shocks and expansion fans, some uncertainty is expected in the results obtained. However, the qualitative trends predicted by the k–ϵ turbulence model are of interest.

Results

25–35-Degree Double Cone

The first case corresponds to a Type VI shock interaction as classified by Edney. The cone half-angles are 25 and 35 deg. A series of runs was made at both the low- and high-Reynolds-number operating conditions, with measured stagnation conditions and freestream Mach number given in Table 1. Conditions for the CFD analysis were chosen to fall within the range of experimental values and are also shown in Table 1. Reynolds numbers based on freestream conditions and the model base diameter (0.051 m) are $Re_D = 3.7 \times 10^5$ for the low-Reynolds-number operating condition, and $Re_D = 6.1 \times 10^5$ for the high-Reynolds-number condition. The base diameter was chosen as the relevant length scale based on the work of Maull.[6] Isothermal wall temperatures for the low- and high-Reynolds-number conditions are set at 575 and 585 K, respectively, based on the wall heating estimate from the thermocouples. The computed flows were not sensitive to small ($\pm 10\%$) changes in the wall temperature. All of the computations shown for this case were performed on a 512×512 computational mesh, which was sufficient to provide a grid-converged solution.[11]

Figure 1a shows an experimental schlieren image of the low-Reynolds-number Type VI interaction, enlarged to highlight the interaction region. Schlieren images of the high-Reynolds-number flow are nearly identical and thus are not shown. Although it is difficult to see the fine detail of the flow as a result of the small model size, the major structures can be resolved. Figure 1b shows a computational schlieren image for this case. By comparison of Figs. 1a and 1b, we see that the size of the separation region and the shock angles all match the computation to within experimental resolution. The features of this flow can be best described with the help of a schematic drawing of a viscous Type VI interaction, shown in Fig. 2. The oblique shock from the nose intersects the oblique shocks from the corner of the cones. An expansion fan is emitted from the intersection point and reflects off the body surface. The reflected expansion waves are then deflected as they pass through the shear layer emanating from the intersection point and eventually intersect with and weaken the oblique shock. The waves are also weakly reflected from the shear layer and recompress the flow along the surface of the second cone. There is a small separated flow region at the corner of the cones caused by the adverse pressure gradient. The separation and reattachment shocks can be seen in Fig. 1.

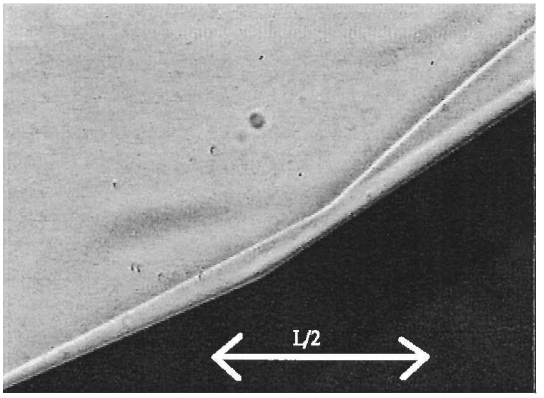

a) Experimental

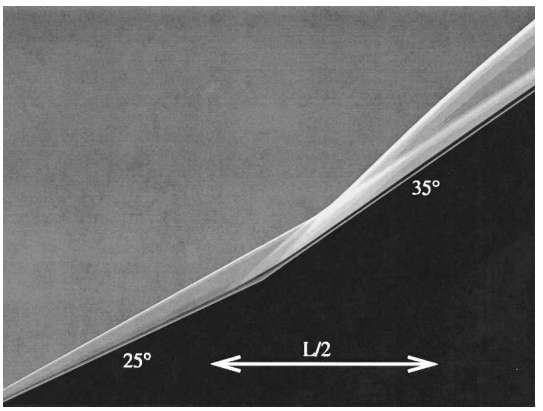

b) Computational

Fig. 1 Schlieren image of a Type VI shock interaction. Double-cone geometry with cone half-angles $\theta_1 = 25$ deg and $\theta_2 = 35$ deg. Air at Mach 8, $T = 57$ K, and $Re_D = 3.7 \times 10^5$.

In these computations we find that the effect of turbulence on the mean flow is negligible. Turbulence affects the mean flow via the turbulent eddy viscosity μ_T, which is added to the molecular viscosity μ in the conservation equations. Thus, the magnitude of μ_T relative to μ is a measure of the effect of turbulence on the flow. For both Type VI shock interactions considered here the ratio μ_T/μ was found to be small compared to one. This is not surprising

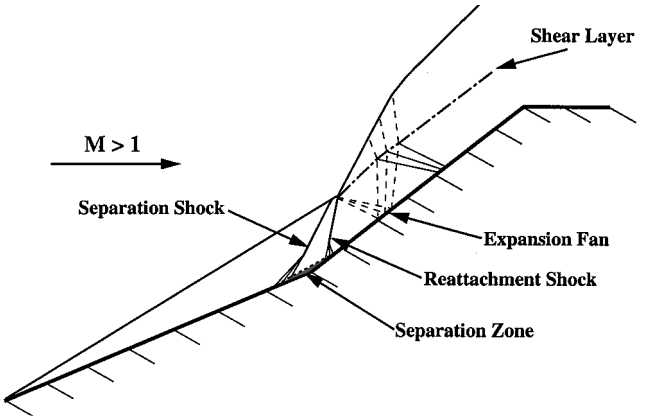

Fig. 2 Schematic diagram of a Type VI shock interaction on a double-cone geometry.

because the maximum local Reynolds number on the surface is an order of magnitude smaller than the transition Reynolds number for a sharp cone in a wind tunnel ($Re_{xt} \sim 3.5 \times 10^6$) (Ref. 23), and the separation and reattachment shocks are too weak to cause boundary-layer transition. In addition, from the schlieren images we see that the shear layer emanating from the triple point appears to be steady and laminar, as is expected because the flow gradients across the shear layer are small and the flow on each side is entirely supersonic. Therefore, the flow solution computed using the k–ϵ turbulence model is essentially identical to the laminar solution.

Figure 3 shows the experimental and computed normalized surface pressure for the low- and high-Reynolds-number cases. Although the CFD results for the two cases are very close, the normalized surface pressure for the high-Reynolds-number flow is about 1.5% higher along the entire surface. This is entirely caused by the fact that the freestream Mach number is slightly higher for the high-Reynolds-number case, as shown in Table 1. Theoretical values for inviscid cone flow with no impingement can be calculated by numerical integration of the Taylor–Maccoll equation[24] and are shown in Fig. 3 for comparison. As expected, the surface pressure on the first cone face before separation is slightly higher than that predicted by the Taylor–Maccoll equation because of boundary-layer displacement, which slightly increases the apparent cone angle seen by the freestream flow. Based on this analysis, the experimental data from the first tap for the high-Reynolds-number runs are too low. The reasons for this low reading are not clear. The first small rise in surface pressure corresponds to the separation point. The second pressure tap ($s/L = 1.0$) is located within the separated flow region, and all four readings are in good agreement with the computations. The broad peak at 43 times freestream pressure corresponds to the flow downstream of the reattachment shock. The third pressure tap ($s/L = 1.25$) is located in this peak region, and again the experimental data match well with the CFD. The surface pressure then decreases as the expansion fan strikes the body and is reflected. The final tap ($s/L = 1.75$) is located on the second cone face well after the reflection of the expansion fan and thus should record a pressure slightly higher than the Taylor–Maccoll value for an inviscid 35-deg cone with no shock impingement. Once again, all four measurements agree well with the CFD data and theoretical results.

The computed size of the separated flow region can be obtained by locating zeros in the wall stress. To determine the size of the separation region in the experiments, the computed separation and reattachment points are first located on the corresponding computational schlieren images. An estimate of the extent of the separation region in the experiment can then be made by carefully comparing flow features and locating the corresponding points on the experimental schlieren images. By using this inverse location technique, we can size the separation region more precisely than by examination of the experimental schlieren images alone. The error in this measurement is estimated from the uncertainty in locating these points. The results are shown in Table 2. The experiments and computation are in good agreement, and both show a slight increase

Table 2 Measured separation and reattachment points (in terms of s/L) for the 25–35-deg double-cone runs

	Low Reynolds number		High Reynolds number	
Location	Experiment	CFD	Experiment	CFD
Separation	0.92 ± 0.02	0.94	0.91 ± 0.02	0.93
Reattachment	1.08 ± 0.02	1.07	1.08 ± 0.02	1.08

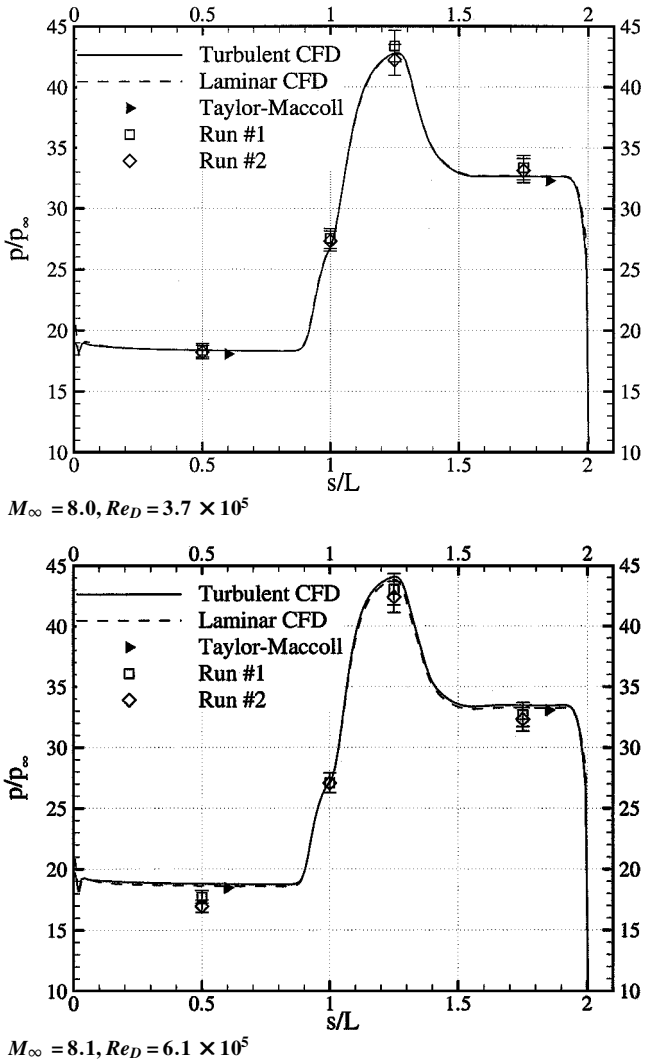

Fig. 3 Computed and experimental surface pressures for two Type VI shock interactions on a double-cone geometry with cone half-angles $\theta_1 = 25$ deg and $\theta_2 = 35$ deg. Values plotted vs distance along the cone surface, normalized by the length of the cone face. Air at $T = 57$ K.

in the size of the separation region for the high-Reynolds-number flow. This is in accordance with Delery,[25] who states that, for a fully laminar interaction, increasing the Reynolds number always results in an increase in the size of the separation zone.

25–50-Degree Double Cone

As the second cone half-angle is increased, an angle will be reached where a Type VI interaction is no longer possible and a Type V interaction occurs. At this point the freestream flow can no longer be turned with an oblique shock on the second cone, and a curved bow shock appears. The second case, with cone half-angles of 25 and 50 deg, falls into this category. As before, a series of runs was made at the low- and high-Reynolds-number operating conditions. The measured stagnation conditions and freestream Mach number are given in Table 3. Reynolds numbers based on the model base diameter are $Re_D = 2.7 \times 10^5$ and 4.8×10^5. The isothermal wall temperatures for the low- and high-Reynolds-number conditions are set at 590 and 630 K, respectively. The experimentally

Table 3 Measured average stagnation and operating conditions for the 25–50-deg double-cone runs

	Low Reynolds number			High Reynolds number		
Variable	Run 1	Run 2	CFD	Run 1	Run 2	CFD
T_0, K	788 ± 8	784 ± 7	786	804 ± 7	802 ± 6	803
p_0, MPa	3.51 ± 0.12	3.32 ± 0.09	3.48	6.57 ± 0.01	6.59 ± 0.02	6.58
M_∞	7.98 ± 0.04	7.98 ± 0.04	8.00	8.07 ± 0.04	8.09 ± 0.04	8.10

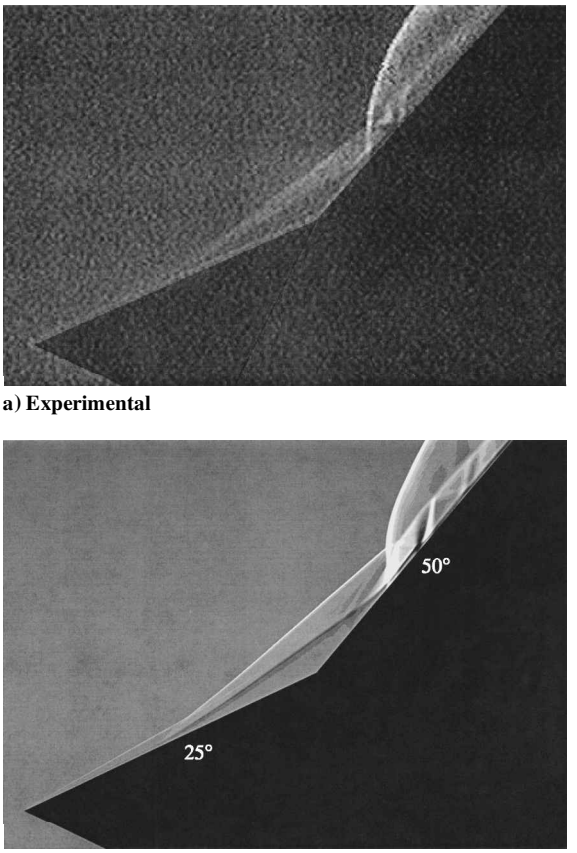

a) Experimental

b) Computational

Fig. 4 Schlieren image of a Type V shock interaction on a double-cone geometry with cone half-angles $\theta_1 = 25$ deg and $\theta_2 = 50$ deg. Air at Mach 8, $T = 57$ K, and $Re_D = 2.7 \times 10^5$.

observed flow exhibited a slight unsteadiness in the shock structure, discussed in detail by Magruder.[14] The results shown here represent typical schlieren images.

Figure 4a shows an experimental schlieren image of the low-Reynolds-number Type V shock interaction, and Fig. 4b shows a computationally generated schlieren image of the same case, obtained on a 1024×1024 grid. This grid was found to be sufficient to resolve the features of the flow.[11] The experimental schlieren looks qualitatively similar to the computational result. Again, the features of this flow can be best described with the help of a schematic diagram, shown in Fig. 5. The separation zone for this case is much larger than for the Type VI shock interaction and extends approximately halfway from the corner to the nose. The shock formed at the separation point interacts with and steepens the oblique shock from the nose. This oblique shock intersects the bow shock from the second cone, and a third shock is transmitted from the intersection toward the body. The reattachment shock intersects this transmitted shock, forming a secondary triple point. A thick shear layer is emitted from the main intersection point on the bow shock, which separates the outboard flow from the supersonic inboard flow. Finally, a merged shock/expansion wave is transmitted from the secondary triple point and strikes the body surface. The expansion wave reflects off the body and intersects the shear layer, where it is partially transmitted and partially reflected as a compression wave. Further reflections of this wave are also evident in Fig. 4, indicating that

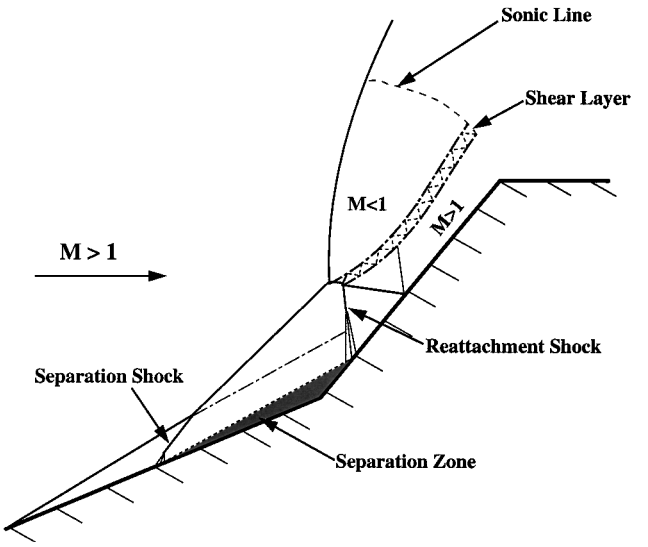

Fig. 5 Schematic diagram of a Type V shock interaction on a double-cone geometry.

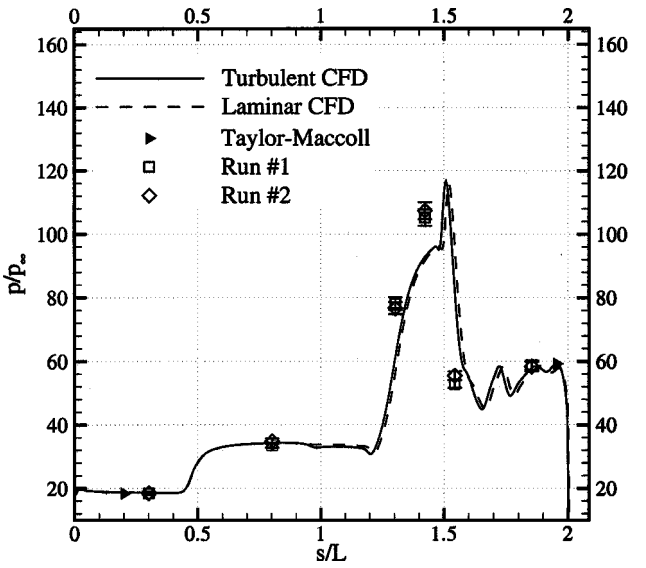

Fig. 6 Computed and experimental surface pressures for a Type V shock interaction on a double-cone geometry with cone half-angles $\theta_1 = 25$ deg and $\theta_2 = 50$ deg. Values plotted vs distance along the cone surface, normalized by the length of the cone face. Air with $T = 57$ K, $M_\infty = 8.0$, and $Re_D = 2.7 \times 10^5$.

steady pressure variations are present on the second cone surface. The turbulent viscosity obtained for this case is very small compared to the molecular viscosity throughout the flow. Thus, the solution obtained using the k–ϵ model is nearly identical to the laminar solution.

The computed and experimental normalized surface pressure for the low-Reynolds-number case are presented in Fig. 6, along with theoretical estimates from the Taylor–Maccoll equation. We see that the laminar and turbulent computations give nearly identical solutions. Both computations agree well with the experimental data on the first cone and in the separation region characterized by the

first pressure plateau. The second pressure rise is caused by the reattachment shock, whereas the highest computed pressure (120 times freestream) corresponds to the regular reflection of the transmitted shock off the cone surface. This is followed by a rapid expansion, and a short series of alternate expansions and recompressions caused by the reflection of the expansion waves between the body surface and the shear layer. These waves create a near-wall flow pattern characteristic of the trapped underexpanded jet flow observed in inviscid Type IV and Type V double-wedge shock interactions. The final abrupt drop in pressure (at $s/L = 2$) is a result of expansion onto the afterbody. The numerical solutions overpredict the size of the separation region, and therefore the reattachment shock and the subsequent features are shifted downstream of the corner as compared to the experimental data. The smaller separation region in the experiment can be caused by transition to turbulent flow because it is well known that the presence of turbulence reduces the size of the separation region. However, because of the limitations on transition prediction with the k–ϵ model pointed out earlier, this effect cannot be accurately reproduced in the CFD.

We next consider the high-Reynolds-number Type V shock interaction. Although this case appears to be qualitatively similar to the low-Reynolds-number interaction just discussed, there are noticeable differences in the effect of turbulence on the flowfield structure. As pointed out earlier, the computed solution for the low-Reynolds-number case shows that the turbulence levels are very low, and the solution obtained using the turbulence model is essentially identical to the laminar solution. In contrast, there is a significant amount of turbulence present in the high-Reynolds-number flow, and thus there are substantial differences between the laminar and turbulent CFD solutions for this case. Figure 7 shows a magnified view of the interaction region in which the fully turbulent area of the flow ($\mu_T > \mu$) is shaded. Also shown are density contours to identify the key features. A 512 × 512 grid was used to obtain these results; the effect of grid refinement will be discussed next. From the figure we see that the k–ϵ model predicts the generation of turbulent viscosity as a result of the adverse pressure gradient of the reattachment and transmitted shocks. Some of this turbulent flow is reversed into the separation region by the recirculation. There are multiple counter-rotating vortices in the separation region; however, the turbulence remains localized in the vortex nearest to the reattachment shock. The flow in the rest of the separation region remains essentially laminar. In addition, the free shear layer emanating from the intersection point and the shear layer enclosing the separation region are also predicted to be laminar. As discussed earlier, turbulent shear layers can require compressibility corrections in the turbulence model. However, addition of these terms would have the effect of delaying transition in the shear layers. Because the shear layers seen here are already predicted to be laminar, addition of the compressibility terms would have no effect on the computed flowfield.

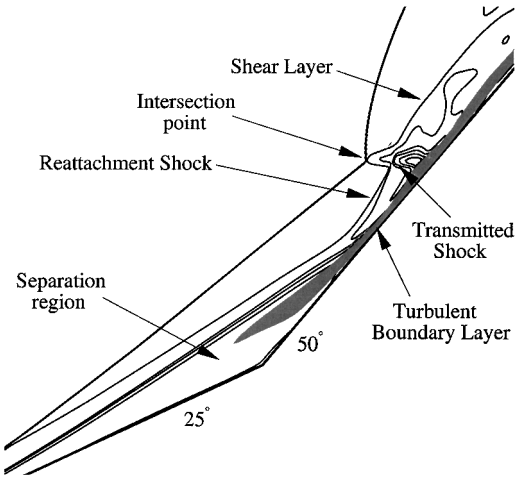

Fig. 7 Turbulent regions in the flow over the 25–50-deg double-cone at $Re_D = 4.8 \times 10^5$. Shaded region corresponds to $\theta_T/\theta_\infty > 1$, and contour lines represent density variation in the flowfield.

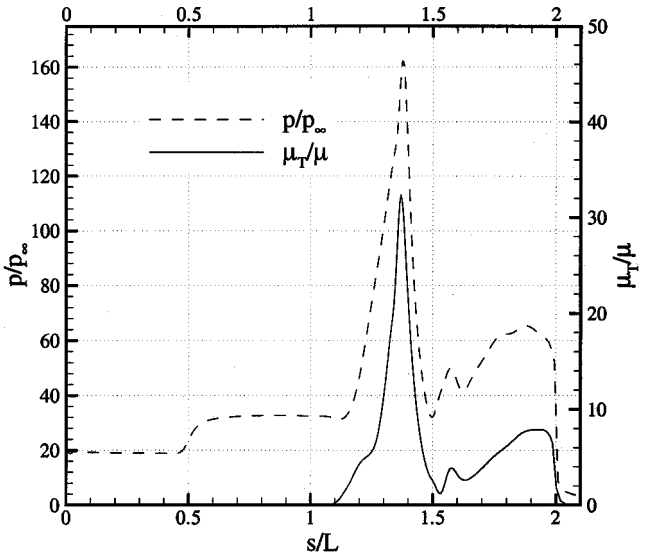

Fig. 8 Computed surface pressure and relative turbulent viscosity on a double-cone geometry with cone half-angles $\theta_1 = 25$ deg and $\theta_2 = 50$ deg. Air with $T = 57$ K, $M_\infty = 8.0$, and $Re_D = 4.8 \times 10^5$.

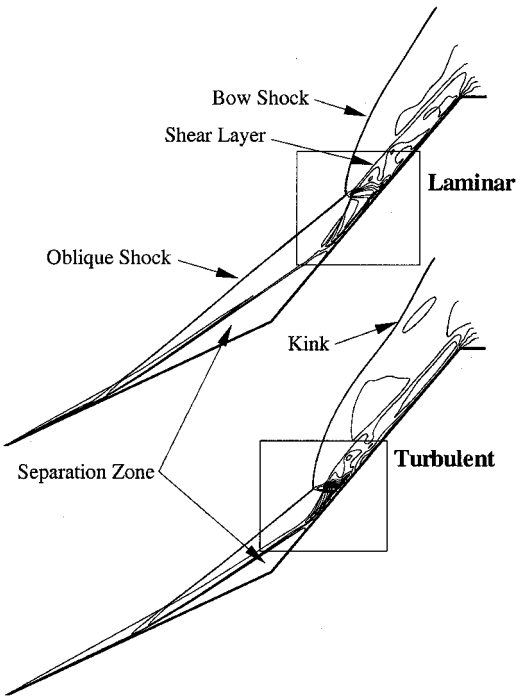

Fig. 9 Effect of turbulence on the flow features in the high-Reynolds-number Type V interaction. Computed density contours on the 512 × 512 grid. Type V shock interaction on a 25–50-deg double-cone at Mach 8, $T = 57$ K, and $Re_D = 4.8 \times 10^5$. Boxes correspond to the magnified view in Fig. 10.

Figure 8 shows the computed variation of μ_T/μ and the normalized pressure at the cone surface. The surface-pressure distribution is qualitatively similar to the low-Reynolds-number case presented in Fig. 6. The variation of the normalized turbulent viscosity shows the increase of turbulence caused by the strong adverse pressure gradient. This is followed by a strong favorable pressure gradient that greatly reduces the turbulence level in the boundary layer. There is further buildup and decrease of turbulence along the second cone corresponding to the recompression and expansion of the gas. Finally, the rapid expansion of the gas onto the afterbody relaminarizes the flow. The boundary layer on the first cone remains entirely laminar, even in the separation region.

Figure 9 compares the computed density contours in the laminar solution with those in the turbulent solution on the same grid.

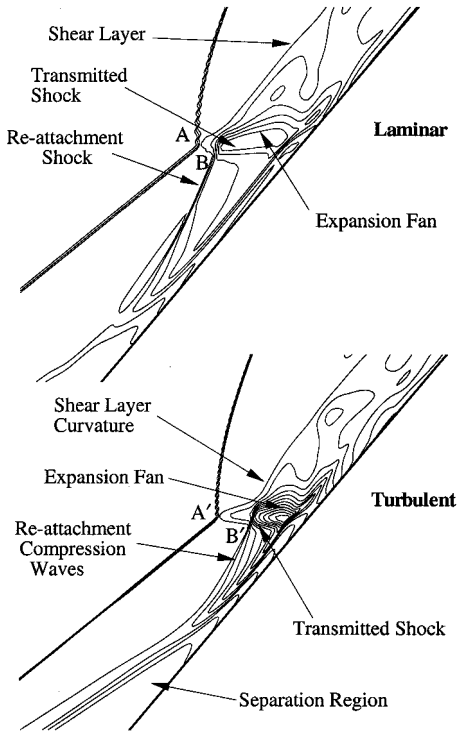

Fig. 10 Effect of turbulence on the flow features in the high-Reynolds-number Type V interaction. Computed density contours on the 512 × 512 grid. Magnified view of the interaction regions shown in Fig. 9.

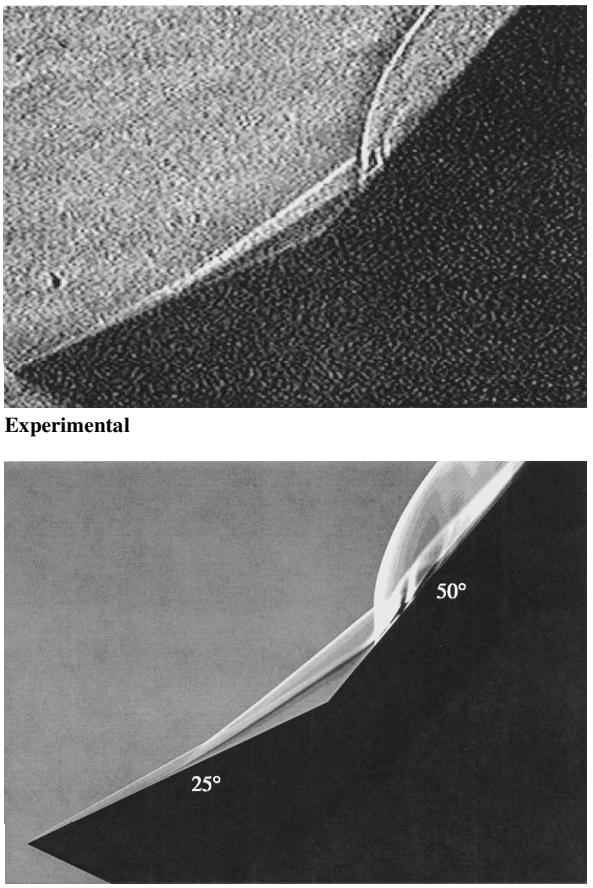

Experimental

Computational

Fig. 11 Schlieren image of a Type V shock interaction on a double-cone geometry with cone half-angles $\theta_1 = 25$ deg and $\theta_2 = 50$ deg. Air at Mach 8, $T = 57$ K, and $Re_D = 4.8 \times 10^5$.

Figure 10 is an enlargement of the interaction region for these cases. In Fig. 9 the flow reattaches earlier in the turbulent case. This alters the location of the shear layer enclosing the separation region. As a result, the turbulent flow separates later than the laminar flow even though the boundary layer is completely laminar on the first cone. Thus turbulence significantly reduces the overall size of the separation region. Figure 10 also shows that the shock structure in the interaction region is affected by turbulence as well. For example, the triple points (A and B in Fig. 10) move closer to the cone surface in the turbulent flow. The compression waves created by the incipient reattachment of the flow on the second cone face coalesce to form the reattachment shock in the laminar solution. However, in the turbulent case these compression waves reach the secondary triple point B' before the shock has formed. In addition, the shock and the expansion fan transmitted from B toward the cone surface are stronger in the turbulent case. This results in a higher peak surface pressure behind the transmitted shock and thus a stronger downstream underexpansion for the turbulent case. The amount of underexpansion in the inboard flow can also affect the global shock shape as a result of the transmission of compression or expansion waves through the shear layer into the outboard flow. One example of this is the characteristic "kink," or change in curvature of the bow shock, visible in Fig. 9. This kink is much more prominent in the turbulent flow because the compression waves that cause it are stronger. Thus, we see that a small change in turbulence intensity near the reattachment point can have a large effect on the overall flow structure as a result of a complex feedback mechanism between the size of the separation zone and the shock structure in the interaction region.

Figure 11 shows experimental and computational schlieren images for this case. The primary visible difference between the high-Reynolds-number case shown here and the low-Reynolds-number case shown in Fig. 4 is the separation region, which is much smaller for the high-Reynolds-number flow. Hefner et al.[26] examined similar interactions on axisymmetric compression corner flows at Mach 5. Hefner demonstrated that for transitional interactions the extent of the separation zone decreases with increasing Reynolds number, the opposite of the trend for laminar or fully turbulent flows. This is the trend observed in these experiments, and the turbulent computations presented here reproduce this effect, indicating that the experiments bracket the transition regime for this flow.

As pointed out earlier, the solutions just presented were obtained on a 512 × 512 grid. The normalized surface pressure computed on this grid for laminar flow is presented in Fig. 12a, as well as results obtained on three other grids. The solution changes significantly from the coarsest to the finest grid. However, there is little difference between the pressure data obtained on the finest two grids (512 × 512 and 1024 × 1024). Thus, the solution obtained on the 512 × 512 grid is close to the grid converged answer. A similar comparison was made for the turbulent computations, with the results presented in Fig. 12b. A 1024 × 1024 grid was not attempted for the turbulent case because of computational limitations. However, based on the laminar results shown here and in Ref. 11 we believe that a grid of 512 × 512 points will provide a turbulent solution that is nearly grid converged. There is some unsteadiness observed in the turbulent computation. The peak pressure varies by about ±5%, and a similar variation is seen in the pressure distribution on the second cone. The unsteadiness in the shock structure and the locations of the separation and reattachment points are much smaller.

The computed and experimental surface pressure are compared in Fig. 13. The laminar solution was obtained on the 1024 × 1024 grid, whereas the turbulent data correspond to the solution obtained on a 512 × 512 grid. Theoretical estimates from the Taylor–Maccoll equation are also shown. The computed pressure on the first cone (before separation) is very close to the Taylor–Maccoll value. However, the experimental data are slightly lower. At the second pressure tap ($s/L = 0.80$), located in the separation region, the turbulent solution is closer to the experiment than the laminar value. The next pressure tap ($s/L = 1.30$) measures the pressure rise caused by the transmitted shock. The turbulent computation reproduces this high-pressure value (165 time freestream), but the location of the peak is shifted slightly downstream. In contrast, the laminar computations

Table 4 Measured separation and reattachment points (in terms of *s/L*) for the 25–50-deg double-cone runs

	Low Reynolds number		High Reynolds number		
Location	Experiment	CFD	Experiment	Laminar CFD	Turbulent CFD
Separation	0.46 ± 0.02	0.47	0.52 ± 0.02	0.34	0.50 ± 0.01
Reattachment	1.43 ± 0.02	1.52	1.29 ± 0.02	1.59	1.37 ± 0.01

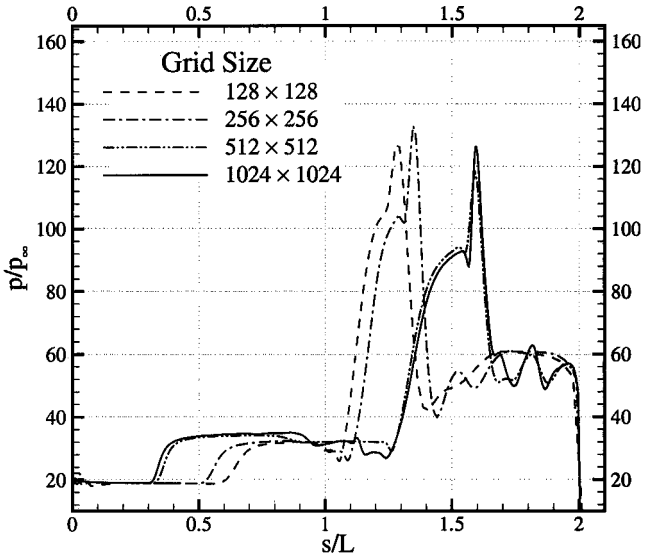

a) Laminar solution

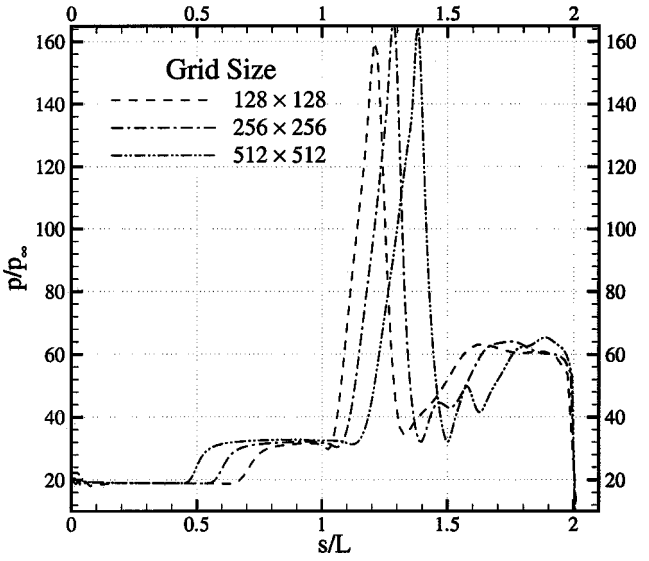

b) Turbulent solution

Fig. 12 Grid refinement study for the Type V shock interaction on a 25–50-deg double-cone at Mach 8.1, $T = 57$ K, and $Re_D = 4.8 \times 10^5$.

predict a much lower peak pressure (125 times freestream) and a much larger separation region. The dramatic differences between the laminar and turbulent solutions for this case are a result of the sensitivity of the interaction to turbulence levels near the triple point, as discussed earlier. The laminar solution shows two distinct pressure rises on the second cone corresponding to the reattachment and transmitted shocks. However, in the turbulent solution the two pressure rises are indistinguishable from each other. The remaining three pressure taps bracket the alternate expansion and recompression region on the second cone. Here again, the turbulent solution is close to the experimental data.

Finally, an estimate of the size of the separation region is presented in Table 4. The laminar computations overpredict the size of the separation region by a large amount, whereas the turbulent predictions are much closer to the experimental estimates. Also shown

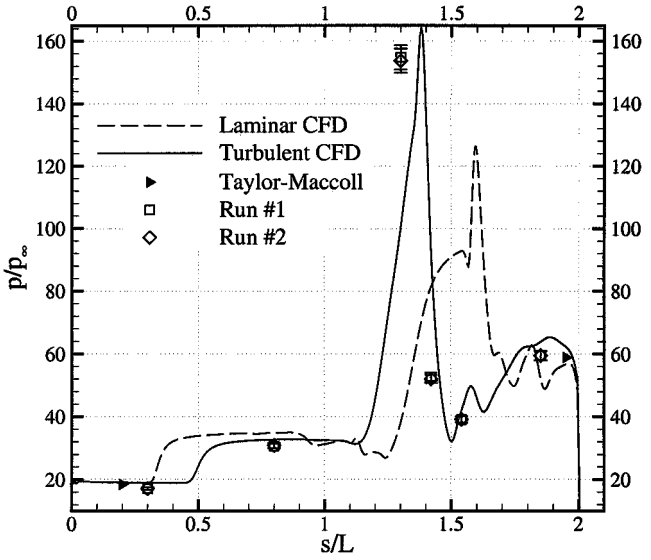

Fig. 13 Computed and experimental surface pressures for a Type V shock interaction on a double-cone geometry with cone half-angles $\theta_1 = 25$ deg and $\theta_2 = 50$ deg. Values plotted vs distance along the cone surface, normalized by the length of the cone face. Air with $T = 57$ K, $M_\infty = 8.1$, and $Re_D = 4.8 \times 10^5$.

is the uncertainty in the location of the separation and reattachment points caused by the slight unsteadiness in the turbulent solution.

Conclusions

We have conducted a series of experiments in the Princeton University Mach 8 Wind Tunnel to study shock interactions on double-cone geometries. Two models, which produced steady Type VI and Type V shock interactions, were tested. The models were instrumented with pressure taps and thermocouples, although the thermocouples were used only to estimate the isothermal wall temperature. Schlieren videos were taken, and images from these videos were compared to laminar and turbulent computational fluid dynamics calculations.

The comparison between the experiments and the computations is excellent for the Type VI shock interaction, where the CFD accurately reproduces the size of the small separation zone and the surface pressure. The computations for the low-Reynolds-number Type V interaction also compare well with the experiments, although the computation slightly overpredicts the location of the reattachment point. The computations for each of these cases demonstrate that the flows are essentially laminar.

Experimental results for the high-Reynolds-number Type V interaction show that the size of the separation region is much smaller than that for the low-Reynolds-number case. This is in contrast to the expected result for laminar or fully turbulent flow. Laminar CFD calculations for this case show a large increase in the size of the separation region, as expected, and thus do not compare well with the experimental data. The turbulent solution shows much better agreement with the experimental data, both in the size of the separation region and the predicted surface pressure. Thus, within the limitations of the k–ϵ turbulence model the computations reproduce the experiment very well.

In addition, both the experimental and computational results from the Type V shock interactions show evidence of alternate compressions and reexpansions along the body surface, similar to those

observed for certain inviscid double-wedge shock interactions. This flow pattern, caused by an underexpanded jet trapped against the body surface by the subsonic external flow, has not previously been observed experimentally in shock interaction flows.

Acknowledgments

This work was supported by Army Research Office Grant DA/DAAH04-95-1-0540, Air Force Office of Scientific Research Contracts F49620-97-1-0181 and F49620-97-1-0484, and the Army High Performance Computing Research Center under the auspices of the Department of the Army, Army Research Laboratory Cooperative Agreement DAAH04-95-2-0003/Contract DAAH04-95-C-0008, the content of which does not necessarily reflect the position or the policy of the government, and no official endorsement should be inferred. Computer time was in part provided by the University of Minnesota Supercomputing Institute.

References

[1]Edney, B., "Anomalous Heat Transfer and Pressure Distributions on Blunt Bodies at Hypersonic Speeds in the Presence of an Impinging Shock," Aeronautical Research Inst. of Sweden, Rept. 115, Stockholm, 1968.

[2]Olejniczak, J., Candler, G. V., Wright, M. J., Levya, I. A., and Hornung, H. G., "Experimental and Computational Study of High Enthalpy Double-Wedge Flows," *Journal of Thermophysics and Heat Transfer,* Vol. 13, No. 4, 1999, pp. 431–440.

[3]Olejniczak, J., Wright, M. J., and Candler, G. V., "Numerical Study of Shock Interactions on Double-Wedge Geometries," AIAA Paper 96-0041, Jan. 1996.

[4]Olejniczak, J., Wright, M. J., and Candler, G. V., "Numerical Study of Inviscid Shock Interactions on Double-Wedge Geometries," *Journal of Fluid Mechanics,* Vol. 352, 1997, pp. 1–25.

[5]Lamont, P. J., and Hunt, B. L., "The Impingement of Underexpanded Axisymmetric Jets on Perpendicular and Inclined Plates," *Journal of Fluid Mechanics,* Vol. 100, No. 3, 1980, pp. 471–511.

[6]Maull, D. J., "Hypersonic Flow over Axially Symmetric Spiked Bodies," *Journal of Fluid Mechanics,* Vol. 8, No. 4, 1960, pp. 584–592.

[7]Bertin, J. J., and Hinkle, J. C., "Experimental Investigation of Supersonic Flow Past Double Wedge Configurations," *AIAA Journal,* Vol. 13, No. 7, 1975, pp. 897–901.

[8]Holden, M. S., and Moselle, J. R., "Theoretical and Experimental Studies of the Shock Wave-Boundary Layer Interaction on Compression Surfaces in Hypersonic Flow," Aerospace Research Lab., TR ARL 70-0002, Wright–Patterson AFB, OH, Jan. 1970.

[9]Holden, M. S., "A Study of Flow Separation in Regions of Shock Wave-Boundary Layer Interaction in Hypersonic Flow," AIAA Paper 78-1169, June 1978.

[10]Baumgartner, M. L., Smits, A. J., Nau, T., and Rowley, C. W., "A New Hypersonic Boundary Layer Facility," AIAA Paper 95-0787, Jan. 1995.

[11]Wright, M. J., Olejniczak, J., Candler, G. V., Magruder, T. D., and Smits, A. J., "Numerical and Experimental Investigation of Double-Cone Shock Interactions," AIAA Paper 97-0063, Jan. 1997.

[12]Livesey, J. L., Jackson, J. D., and Southern, C. J., "The Static Hole Error Problem—An Experimental Investigation of Errors for Holes of Varying Diameters and Depths," *Aircraft Engineering,* Vol. 34, No. 396, 1962, pp. 43–47.

[13]Merzkirch, W., *Flow Visualization*, Academic Press, Orlando, FL, 1987, pp. 115–218.

[14]Magruder, T. D., "An Experimental Study of Shock/Shock and Shock/Boundary Layer Interactions on Double-Cone Geometries in Hypersonic Flow," M.S. Thesis, Dept. of Mechanical and Aerospace Engineering, Princeton Univ., Princeton, NJ, Nov. 1997.

[15]Wilcox, D. C., *Turbulence Modeling for CFD*, DCW Industries, Inc., La Cañada, CA, 1993, p. 180.

[16]Jones, W. P., and Launder, B. E., "The Prediction of Laminarization with a Two-Equation Model of Turbulence," *International Journal of Heat and Mass Transfer*, Vol. 15, No. 2, 1972, pp. 301–314.

[17]Yates, L., "Images Constructed from Computed Flowfields," *AIAA Journal,* Vol. 31, No. 10, 1993, pp. 1877–1884.

[18]MacCormack, R. W., and Candler, G. V., "The Solution of the Navier–Stokes Equations Using Gauss–Seidel Line Relaxation," *Computers and Fluids,* Vol. 17, No. 1, 1989, pp. 135–150.

[19]Sinha, K., and Candler, G. V., "An Accurate Implicit Formulation of a Two-Equation Turbulence Model," AIAA Paper 98-2649, June 1998.

[20]Wright, M. J., Candler, G. V., and Bose, D., "Data-Parallel Line Relaxation Method for the Navier–Stokes Equations," *AIAA Journal,* Vol. 36, No. 9, 1998, pp. 1603–1609.

[21]Zhang, H. S., So, R. M. C., Speziale, C. G., and Lai, Y. G., "A Near-Wall Two-Equation Model for Compressible Turbulent Flows," AIAA Paper 92-0442, Jan. 1992.

[22]Birch, S. F., and Keyes, J. W., "Transition in Compressible Free Shear Layers," *Journal of Spacecraft and Rockets,* Vol. 9, No. 8, 1972, pp. 623, 624.

[23]Anderson, J. D., *Hypersonic and High Temperature Gas Dynamics,* McGraw–Hill, New York, 1989, p. 274.

[24]Thompson, P. A., *Compressible Fluid Dynamics*, Rensselaer Polytechnic Inst., Troy, NY, 1988, pp. 487–495.

[25]Delery, J., "Shock/Shock and Shock-Wave/Boundary Layer Interactions in Hypersonic Flows," *Special Course on Aerothermodynamics of Hypersonic Vehicles,* Rept. R-761, AGARD, June 1988.

[26]Hefner, K. S., Chpoun, A., and Lengrand, J. C., "Experimental Study of Transitional Axisymmetric Shock-Boundary Layer Interactions at $M = 5$," AIAA Paper 93-3131, July 1993.

M. Sichel
Associate Editor